CrystEngComm

ROYAL SOCIETY OF CHEMISTRY

PAPER

Cite this: *CrystEngComm*, 2023, **25**, 6102

Interface segregation of iron sintering aid in gadolinium-doped ceria†

Marina Machado, [a] Andre L. da Silva, [b] Leticia P. R. Moraes,[a] Lays N. Rodrigues,[a] Lorena B. Caliman,[b] Douglas Gouvêa[b] and Fabio C. Fonseca *[a]

Received 26th August 2023,
Accepted 10th October 2023

DOI: 10.1039/d3ce00852e

rsc.li/crystengcomm

Sintering additives are commonly used in ceria-based oxide aiming at decreasing temperatures to prevent undesired reactions in several applications such as in solid oxide fuel cell functional layers. The role played by the sintering additive is studied in the case of Fe_2O_3 added to gadolinium-doped ceria (CGO). The distribution of iron on the CGO nanopowders was measured by a simple chemical method. The enhanced sintering of CGO is associated with the preferred segregation of iron species at the grain boundaries. Nevertheless, iron addition was found to change the distribution of gadolinium in the coprecipitated CGO powders. The saturation of the sintering aid at the grain boundary was induced by increasing the grain size of CGO. The resulting precipitation of iron-rich grains induced a small increase in the electrical conductivity of CGO.

Introduction

Doped ceria has been studied extensively as a material for different electrochemical applications, like solid oxide fuel cells (SOFC), owing to its high oxygen ion conductivity at intermediate temperatures (500–800 °C). Such high oxygen mobility confers to the ceria-based active support's outstanding catalytic performance, due to its high oxygen storage capacity and redox catalytic properties.[1–10] Gadolinium-doped (10–20 mol%) ceria (CGO) is notably one of the most important cerium-based ionic conductors as the aliovalent dopant increases the concentration of mobile oxygen ion vacancies resulting in high oxygen conductivity. Controlling the properties of ceria-based materials requires a full understanding of the high-temperature mass transport and diffusion process taking place on such oxides during both processing and application. Possibly, the main drawback of cerium-based oxides in a multi-layered device is the high sintering temperature (usually ≥1500 °C) needed to obtain a dense layer.[11–15] In addition to representing a costlier process, it can make cofiring of the SOFC unviable due to undesired reactions between the fuel cell components and poor mechanical properties resulting from larger grain size. On the other hand, keeping a high surface area in high-temperature applications, such as in chemical looping and heterogeneous catalysis, in which the catalytic activity of ceria dependence on the active surface area is a major concern in increasing the durability of devices using this material.[16,17] Therefore, the energetics of high-surface-area ceria nanoparticles are of crucial importance for several emerging technologies related to new energies and sustainable development.

Several methods have been investigated to improve the sintering of cerium oxides, generally involving the control of the precursor ceramic powders.[18–20] The main ones include the addition of sintering additives and the control of both the size and the morphology of the material.[21–23] Wet chemistry synthesis usually results in nanometric powders with high sintering activity that promote densification mechanisms. Moreover, the densification temperature can further be reduced by the addition of transition metal oxide (TMO) additives.[24–28] Among the different additives, a particularly interesting TMO is Fe_2O_3, which in addition to acting as a sintering aid, has also been shown to improve the grain boundary conductivity of ceria.[29–31] Additionally, Fe is present in the interconnect material used in SOFCs and metal-supported cells, and it can diffuse through the interfaces into the cell.[32,33] Therefore, it is also important to study how Fe doping can affect the ceria-based components of the fuel cell.

The analysis of the distribution of the dopants in the starting powder of ceria is valuable for understanding the sintering behaviour of ceria and the dopant's distribution after sintering is important to analyse the electrical

[a] *Instituto de Pesquisas Energéticas e Nucleares, IPEN-CNEN/SP, São Paulo, 05508-000, Brazil. E-mail: fabiocf@usp.br*
[b] *Department of Metallurgical and Materials Engineering, Escola Politécnica – University of São Paulo, São Paulo 05508-030, Brazil*

† Electronic supplementary information (ESI) available. See DOI: https://doi.org/10.1039/d3ce00852e

properties of the material. Many studies have investigated TMO-doped CGO. Small amounts (<0.5 mol%) of iron oxide in CGO resulted in no additional phases after ceramic sintering.[34] Cobalt doping modifies the grain boundary conductivity and reduces the sintering temperature of CGO by over 150 °C. However, the cobalt-rich phase segregates[22,35] at the grain boundaries of CGO at low sintering temperatures. Such previous studies have focused on the sintering and conductivity behaviour of TMO-doped CGO, but a more detailed characterization of the distribution of the dopants in the powders is missing. Thus, studying the distribution of the dopants is an important step towards further understanding the effect of the dopants on the CGO properties.

The sintering additive added to a nano-oxide can follow distinct paths: form a solid solution, segregate at interfaces, or precipitate a second phase. However, the exact path varies from system to system, and the relationship between the amount of additive and the preferred equilibrium state cannot be predicted with certainty. The extension of the bulk solubility, for instance, relies on the enthalpy of mixing, the enthalpy of segregation, and the availability of the grain boundaries (GB) since the total energy of the system accounts for the bulk volume and the total interfacial areas.[36] The enthalpy of interface segregation (ΔH_{seg}) (eqn (1)) can be associated with different parameters such as the difference in interface energy between the dopant and the host (ΔH_{σ}), the elastic solute strain energy owing to the size difference between the dopant and host ions (ΔH_{ε}), the solute–solvent interaction (ΔH_{ω}), and the electrostatic potential/charge compensation (ΔH_{ϕ}).[37,38]

$$\Delta H_{seg} = \Delta H_{\sigma} + \Delta H_{\varepsilon} + \Delta H_{\omega} + \Delta H_{\phi} \quad (1)$$

The additive is expected to segregate at the interface with higher energy to minimize the system's overall energy.[39] Thus, if the dopant preferably segregates at the grain boundary, it will decrease the grain boundary energy, favouring densification. Therefore, the segregation of species in nano-oxides plays a crucial role in the microstructural evolution during sintering.

In this study, the effect of sintering aid segregation on the properties of Fe-doped CGO was investigated. The distribution of the dopant was quantified revealing the mechanisms for enhanced sintering of CGO.

Experimental

Synthesis of Fe-doped CGO nanopowders

A solid solution of gadolinium-doped (10 mol%) ceria (CGO), CGO doped with 1 mol% Fe_2O_3 (1Fe–CGO), and CGO doped with 5 mol% Fe_2O_3 (5Fe–CGO) were synthesized using an aqueous precipitation method.[40] The precursors used were cerium(III) nitrate ($Ce(NO_3)_3{\cdot}6H_2O$, 99%), gadolinium(III) nitrate ($Gd(NO_3)_3{\cdot}6H_2O$, 99.9%), and iron(III) nitrate ($Fe(NO_3)_3{\cdot}9H_2O$, 98%), all from Sigma-Aldrich. First, a 200 ml aqueous solution containing a total of 6 g of the precursors was prepared with stoichiometric amounts of cations. Next, 28 g of hexamethylenetetramine (HMT, 99%, Sigma-Aldrich) was slowly added to the solution under constant stirring for 3 h at 85 °C to obtain the precipitated oxides. The products were collected by centrifugation, washed by successive rounds of centrifugation with water and isopropyl alcohol, dried at 100 °C for 12 h, and then calcined in air at 500 °C for 2 h.

Powder characterization

Powder X-ray diffraction (XRD) patterns were obtained using a Philips X'Pert-MPD diffractometer with Cu K_{α} radiation over the 5–90° 2θ range at 0.02° 2θ steps per second. The diffractograms were analysed using the X'Pert Highscore software to calculate the lattice parameters and crystallite sizes *via* the Rietveld method, using $MgAl_2O_4$ as a standard.

The chemical compositions were determined by inductively coupled plasma atomic emission optical spectroscopy (ICP-OES) using a Spectro Across spectrometer. Powder densities were determined using a Micrometrics AccuPyc II 1340 gas pycnometer after degassing with 200 purges. The specific surface areas (SSAs) of the samples were determined by nitrogen gas adsorption measurements (at 77 K) (Micromeritics Gemini VII) according to the Brunauer–Emmett–Teller (BET) method. Before the analysis, all samples were degassed under vacuum at 300 °C for ~18 h using a Micromeritics VacPrep 061. The morphology of the powders was analysed by scanning transmission electron microscopy (STEM) using a JEM-2100 (JEOL) microscope operating with a parallel beam at 200 kV, equipped with a 4k × 4k (TVIPS) camera. The distribution of the atomic elements of the CGO and 5Fe–CGO samples was qualitatively analysed using electron energy loss spectroscopy (EELS) mapping images.

Cylindrical pellets of 6 mm in diameter of CGO, 1Fe–CGO, and 5Fe–CGO were prepared by uniaxial pressing (1000 kgf cm^{-2}) and sintered at 1200 °C and 1400 °C with 1 h dwelling time. The microstructures of the sintered samples were analysed by scanning electron microscopy (SEM, Inspect F50) with a secondary and backscattered electron detector. The SEM analyses were conducted on polished and thermally etched surfaces (1100 °C and 1300 °C for the samples sintered at 1200 °C and 1400 °C, respectively). The average grain sizes were evaluated using the ImageJ software. The energy dispersive spectroscopy (EDS) elemental mapping of the CGO samples sintered at 1400 °C was performed with the SEM JSM-6010LA microscope.

Surface segregation

The surface excess of Fe_2O_3 in CGO nanoparticles was determined by the superficial lixiviation method following a protocol described elsewhere.[39,41,42] Typically, the experiment was performed by ultrasonicating ~100 mg of the as-prepared powder with 2 g of 0.1 M HNO_3 solution (pH = 1) for 1 h. The separation of the supernatant and the powder

was carried out by centrifugation at 13 000 rpm for 1 h. Subsequently, ~1 g of the supernatant solution was collected and diluted in ~10 g of H_2O. These solutions were analysed by ICP-OES to determine the precise composition, providing the quantity of lixiviated ions from the surface of the nanoparticles.

Thermo-mechanical and electrochemical characterization

Cylindrical pellets of 6 mm in diameter of CGO, 1Fe–CGO, and 5Fe–CGO were prepared by uniaxial pressing (1000 kgf cm^{-2}) for dilatometry analysis (TMA). The TMA runs were carried out using the Setaram Labsys equipment between room temperature and 1400 °C with a heating rate of 10 °C min^{-1} under a synthetic air flow of 50 ml min^{-1}.

The electrical properties of cylindrical pellets (typically, 10 mm diameter and 2 mm thick) sintered at 1400 °C for 1 h were analysed by electrochemical impedance spectroscopy measurements (EIS), under a synthetic air flow, in the temperature range of 300–800 °C.[43] The impedance measurements were performed using the Novocontrol frequency analyser (Alpha A), using a frequency between 10 MHz and 1 Hz and an AC amplitude of 100 mV. A high-purity gold paste was used to prepare the electrodes in the Au/CGO/Au symmetric cell configuration. The collected diagrams were analysed with the ZView software. The total resistance was measured by EIS, including both the bulk and grain boundary contributions, and the total conductivity values were calculated by normalizing the dimensions of the sample.

Results and discussion

Powder characterization

The chemical composition data of the CGO powders analysed by ICP-OES are shown in Table 1. The results show that the measured amount of gadolinium and iron were close to the nominal ones.

The X-ray diffraction (XRD) patterns of the calcined samples are shown in Fig. 1. The diffractograms were indexed to the single-phase fluorite structure of ceria (ICDD 96-900-9009). No second phase was detected by XRD, suggesting that both gadolinium and iron were either dissolved in a solid solution or segregated at the interfaces of the ceria nanoparticles. Broad peaks typical of nanosized crystallites can be observed. Increasing the Fe content resulted in a greater broadening of the diffraction peaks, indicating a decrease in crystallite sizes, as shown in Table 2.

Table 1 Chemical composition of the Fe-doped CGO powders determined by ICP-OES

Sample	Fe (mol%)	Gd (mol%)	Fe_2O_3 (mol%)	Gd_2O_3 (mol%)
CGO	0.0	10.6	0.0	5.3
1Fe–CGO	3.0	10.4	1.5	5.2
5Fe–CGO	8.8	9.0	4.4	4.5

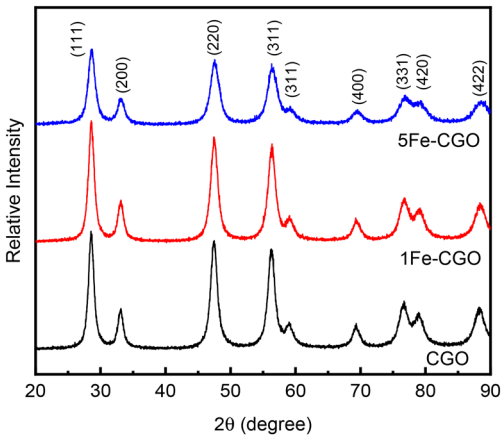

Fig. 1 X-ray diffraction patterns of CGO and Fe-doped CGO.

By using the XRD and BET data, the crystallite size, lattice parameter, density, specific surface area (SSA), total specific surface area (TSA), specific GB interface area (SGB), and SGB/SSA ratio of the samples were determined, as listed in Table 2. The crystallite sizes decreased as the iron content increased, a feature associated with the effect of segregated dopants on reducing the interfacial energies.[44–47] According to coarsening models, during the isothermal growth of nanoparticles, the average particle size (d_t) dependence with time (t) follows a general law of growth (eqn (2)).

$$d_t^n - d_0^n = kD\sigma_i(t - t_0) \quad (2)$$

where d_0 is the average particle size at t_0; D is the diffusion coefficient; σ is the interfacial energy; k is a constant that depends on the approach to develop the kinetic equation; the exponent n = 2, 3, …, generally reflecting the growth mechanism.[48] According to eqn (2), a small crystallite size can be favoured at a given temperature if the σ_i is reduced.

The reduction in interfacial energy is intrinsically connected to interfacial segregation as described in eqn (3), which is based on an extension of the Gibbs adsorption isotherm.[49,50]

$$\sigma_i = \sigma_0 - \Gamma_i \Delta H_{seg} \quad (3)$$

where σ_i is the interface energy of the doped material, σ_0 represents the interface energy of the undoped material, ΔH_{seg} is the enthalpy of segregation, and Γ_i is the solute excess at the interface, expressed by n/A, in which n is the amount of the component at the interface and A is the interface area. eqn (3) holds for both the solid–gas (surface) and solid–solid (grain boundary) interfaces. However, such a relation is strictly valid for systems with a single-phase and low concentration of dopants.[39] Based on eqn (2) and (3), and the decrease in the crystallite size upon Fe addition, it is possible to expect that the interface excess is likely to take place in the Fe-doped CGO samples.

Table 2 Crystallite sizes, lattice parameters, density, specific surface area (SSA), total specific area (TSA), specific GB area (SGB), and GB/SSA ratio of CGO and Fe-doped CGO samples

Sample	Crystallite sizes (nm)	Lattice parameters (Å)	Density (g cm^{-3})	Specific surface area (m^2 g^{-1})	Total specific area (m^2 g^{-1})	Specific grain boundary area (m^2 g^{-1})	SGB/SSA ratio
CGO	8.5 ± 0.1	5.4277 ± 0.0017	5.397 ± 0.027	111.4 ± 0.6	154.8 ± 1.7	21.7 ± 0.9	0.19 ± 0.01
1Fe–CGO	7.8 ± 0.1	5.4213 ± 0.0016	5.366 ± 0.012	106.9 ± 0.5	169.6 ± 1.9	31.4 ± 1.0	0.29 ± 0.01
5Fe–CGO	6.5 ± 0.1	5.4144 ± 0.0020	4.746 ± 0.020	108.1 ± 0.5	230.1 ± 3.1	61.0 ± 1.6	0.56 ± 0.01

The calculated cubic lattice parameter of the CGO sample was 5.4277 ± 0.0017 Å. The CGO lattice parameter is slightly higher than that of CeO_2 (a = 5.4110 Å, ICDD 96-900-9009). Such lattice expansion is due to the difference in the ionic radius of Gd^{3+} (0.105 nm) and Ce^{4+} (0.097 nm) with coordination number VIII.[27] Previous studies of similar CGO samples have reported lattice parameters in the range of 5.4166 Å to 5.42 Å.[27,51–53] The lattice parameters of Fe-doped CGO linearly decreased as the amount of iron increased in the sample. This linear relationship can be fitted as $a = 5.427 - 0.1733x$. It is interesting to note that the CGO lattice parameter dependence on the gadolinium content usually deviates from a linear Vegard-type relationship.[54] The observed decrease in the lattice parameter is possibly attributed to the smaller radius of Fe^{3+} (0.078 nm) than that of both Ce^{4+} (0.097 nm) and Gd^{3+} (0.105 nm).[39,52]

The density values of the Fe–CGO powders measured by gas pycnometry are shown in Table 2. The pycnometer uses the gas displacement method to accurately measure the volume of the sample. The measurement procedure includes consecutive purges to ensure a clean surface, free of water and other possible adsorbed species before data collection. The measured density of the CGO powder (5.397 g cm^{-3}) was much lower than the ~7.2 g cm^{-3} theoretical density (CeO_2 – 7.22 g cm^{-3}; Gd_2O_3 – 7.41 g cm^{-3}). On the other hand, the density of the CGO sample calculated from XRD data was 7.149 g cm^{-3}. Such a difference suggests that the pycnometer density is possibly affected by the surface of the nanoparticles. The density of nano-oxides with small crystallite sizes (≤20 nm) has been reported to exhibit lower values than the theoretical ones.[39,42,55] Such an effect is still unclear, but it was attributed to a structural disorder related to a low-density superficial layer in nanoparticles.[38] Since the surface of nanocrystalline oxides represents a high percentage of the total volume of the particle, surfaces with a high number of defects are likely to induce a decrease in the overall density of the material. This effect is more pronounced in the Fe-doped samples 1Fe–CGO and 5Fe–CGO, which have measured densities of 5.366 g cm^{-3} and 4.746 g cm^{-3}, respectively. Fe doping can contribute to the decrease in the density of CGO because of the lower theoretical density of iron oxide (5.24 g cm^{-3}). However, the lower density of the Fe-doped CGO is likely to be related to the effect of the decreased crystallite size due to the segregated iron cations on the surface of the ceria particles.

The specific surface areas of the CGO, 1Fe–CGO, and 5Fe–CGO samples were 111.4, 106.9, and 108.1 m^2 g^{-1}, respectively. The addition of iron to the CGO slightly decreased the SSA, which can be associated with the dopant distribution into the CGO matrix. The SSA can also be related to the calculated total specific surface area (TSA) and specific GB interface area (SGB) shown in Table 2. The TSA was calculated using eqn (4), assuming tetrakaidecahedral grains, by:

$$\mathrm{TSA} = \frac{7.1}{\rho d} \tag{4}$$

where ρ is the measured density (Table 2) and d is the crystallite size. The TSAs of all samples were higher than the SSA, indicating that the particles are agglomerated. The higher the difference between SSA and TSA, the higher the specific grain boundary area (SGB), which can be calculated according to eqn (5).

$$\mathrm{SGB} = \frac{(\mathrm{TSA} - \mathrm{SSA})}{2} \tag{5}$$

The (TSA – SSA) difference is divided by two because each grain boundary is shared by at least two grains. The SGB increased as the amount of iron increased in the system. This behaviour indicates a possible preference of the dopant towards the GB segregation. As shown in eqn (3), the interface energy is directly related to interface segregation. Thus, if the SGB area increases, it means that the GB is becoming more thermodynamically stable than the surface, which indicates a reduction in the GB energy and an increase in GB excess.[39,56]

The addition of Fe in the CGO resulted in single-phase compounds, *i.e.*, no secondary phase was detected by XRD (Fig. 2). Therefore, the dopant is either dissolved in solid

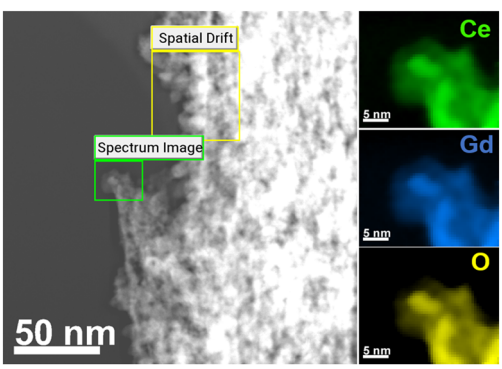

Fig. 2 STEM EELS of CGO.

solution or segregated at the interfaces. Although it is difficult to precisely determine the solubility limit of Fe_2O_3 into CGO nanoparticles, similar systems, *e.g.*, Fe_2O_3-doped SnO_2, pointed out to a very low iron solubility, with the major fraction of the dopant segregated at the grain boundaries.[41]

To further investigate the dopant's distribution on the CGO nanoparticles, the surface segregation was directly measured by using the selective solubility method. Such a surface lixiviation method was previously proposed and tested in similar oxide systems.[48] The method is based on the solubility difference between the dopant and the matrix, in which an acid solution selectively removes the exposed ions at the surface of the nanoparticle. Considering that the acid solution cannot access the ions located in both the GBs and the bulk, it is possible to determine the surface excess by quantifying the ion content in the solution used for the lixiviation of the surface. Following the procedure detailed in the Experimental section, the surface excess (Γ) for the present system was calculated according to eqn (6):

$$\Gamma = n/\mathrm{SSA} \quad (6)$$

where n is the number of moles of dopant lixiviated for each sample.

The surface excess was measured for the three metals presented in this system (Table 3). Only a small amount of cerium was detected in the lixiviated solution, 0.006, 0.060, and 0.076 μmol m^{-2} for CGO, 1Fe–CGO, and 5Fe–CGO respectively, confirming the stability of cerium oxide in nitric acid. It is interesting to observe that ~0.2 μmol m^{-2} of Gd segregated on the surface of CGO nanoparticles, while Fe-doped samples exhibited a larger amount of lixiviated Gd. Thus, the experimental results showed that adding a sintering aid in Gd-doped ceria changes the distribution surface cations and possibly the formation of the ceria : gadolinia solid solution; a feature that influences both the sintering and the electrochemical properties of ceria-based compounds. The Fe^{3+} ion surface excess for 1Fe–CGO was very low (0.007 μmol m^{-2}), suggesting that the main fraction of the dopant was either in a solid solution or segregated at the GBs. However, for the 5Fe–CGO, a pronounced increase in iron concentration (0.139 μmol m^{-2}) was detected on the surface as shown in Table 3. In the Fe–CGO system, upon increasing the iron content from 1 mol% Fe_2O_3, both the bulk and the grain boundary reach saturation and the surface excess Γ rapidly

Table 3 Fe, Gd, and Ce surface excess (Γ) of CGO and Fe-doped CGO samples

	Γ (μmol m^{-2})		
Sample	Fe	Gd	Ce
CGO	0.001 ± 0.000	0.197 ± 0.001	0.006 ± 0.000
1Fe–CGO	0.007 ± 0.000	0.246 ± 0.001	0.060 ± 0.000
5Fe–CGO	0.139 ± 0.001	0.245 ± 0.001	0.076 ± 0.000

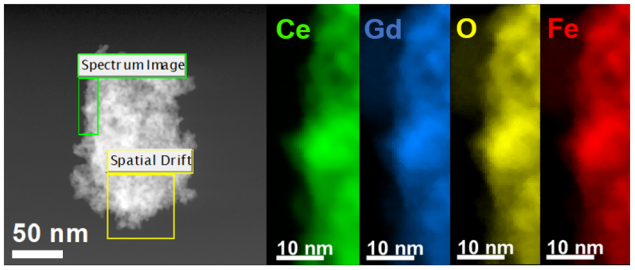

Fig. 3 STEM EELS of 5 mol% Fe-doped CGO.

increases with increasing Fe content. The lixiviation method showed the interaction of Gd and the sintering aid and the distribution of the dopants in the material. Such a distribution has a direct impact on the properties of ionic conductors synthesized using simultaneous doping for ionic conductivity (Gd) and as a sintering aid (Fe).

Fig. 2 and 3 show the STEM-EELS images for CGO and 5Fe–CGO, respectively. The images evidenced that the nanoparticles are highly agglomerated, which confirms the high specific GB area data listed in Table 2. The EELS mapping images show that the atomic elements were homogeneously distributed on the surface of the nanoparticles. For the CGO, iron was not detected, whereas for the 5Fe–CGO sample, iron was equally distributed along with cerium, gadolinium, and oxygen.

The experimental findings show that iron segregated in CGO on the surface and at the GB, the GB being the dominant segregation. The increased GB area observed in the powders doped with 5 mol% Fe_2O_3 suggests that the dopant affects the solid–solid interface (GB) to facilitate the sintering process.

Sintering and electrochemical characterization

The temperature dependence on the linear shrinkage and shrinkage rate profiles for the Fe–CGO samples are shown in

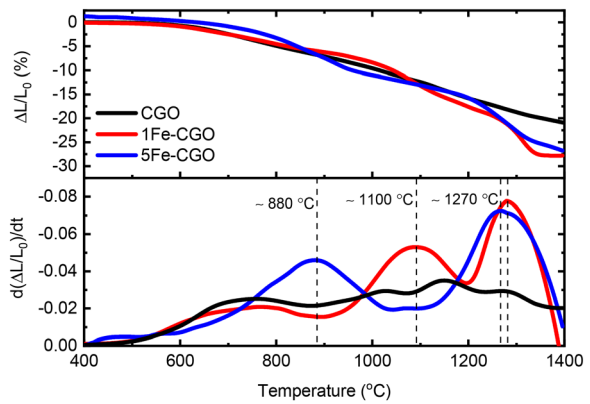

Fig. 4 Linear shrinkage profiles (top) and the differential shrinkage with respect to time (bottom) for CGO, 1Fe–CGO, and 5Fe–CGO samples.

Fig. 4. All samples exhibited an onset of linear shrinkage at ~600 °C. The CGO sample had a temperature-driven retraction of ~20% at 1400 °C while Fe-doped samples had a ~28% retraction at the same sintering temperature. The Fe-doped samples showed two pronounced rate maxima in the shrinkage rate profiles. Such a two-stage densification mechanism is usually observed in composite materials and possibly reflects the segregated iron on the surface of the particles.[20,57] The two well-defined maxima of linear shrinkage rates for Fe-doped samples are associated with the densification and grain growth mechanisms.[58] The 1Fe–CGO sample exhibited the first maximum at ~1100 °C, whereas the 5Fe–CGO had the first significant retraction shifted to a lower temperature (~880 °C). The second maximum of both Fe-doped samples coincides at ~1270 °C. It is observed that with increasing Fe content, the activation energy for densification decreased, as there was a displacement of the peaks of maximum shrinkage (sintering activity) to lower temperatures. The shrinkage profiles suggest a change in the densification mechanism after Fe doping. There is an indication that surface reactivity is increased with Fe doping. Such an effect is related to the segregation of iron at the grain boundary interface, minimizing the GB energy and favouring the elimination of high-energy solid–gas interface leading to densification. From the experimental results, it is verified that the addition of small amounts of Fe alters the sintering mechanism, increasing the densification rate and reducing the CGO sintering temperature.

To further study the effect of Fe doping on CGO, a temperature close to the maximum activity of the CGO sample was chosen, *i.e.*, T = 1200 °C. Fig. 5 shows the microstructure of the polished and thermally etched samples sintered at 1200 °C. The observed features agree with the discussed densification processes based on dilatometric analysis (Fig. 4). The CGO sample sintered at 1200 °C

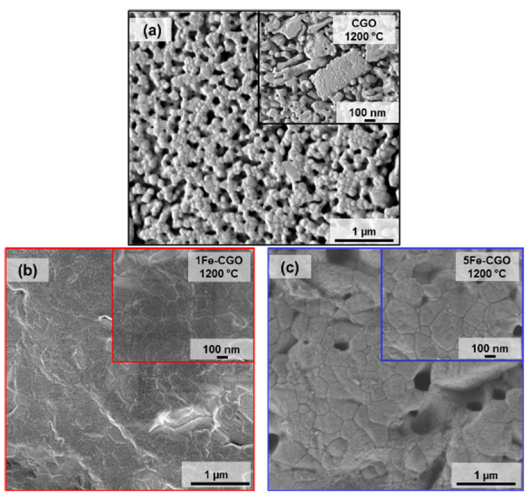

Fig. 5 SEM images of polished and thermally etched cross-sections of (a) CCO, (b) 1Fe–CGO and (c) 5Fe–CGO, sintered at 1200 °C. Insets show a higher magnification region.

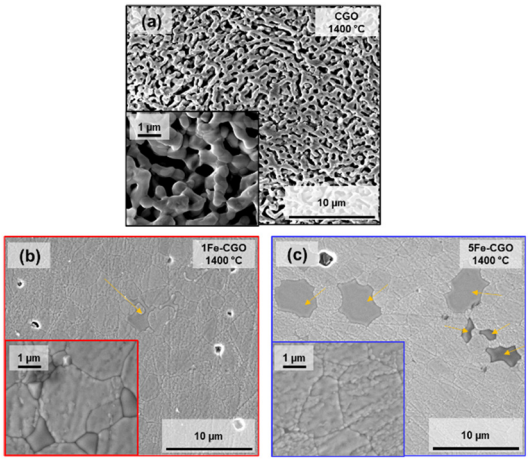

Fig. 6 SEM images of polished and thermally etched cross-sections of (a) CGO, (b) 1Fe–CGO and (c) 5Fe–CGO, all sintered at 1400 °C. Insets show a higher magnification.

(Fig. 5a) exhibited a porous structure with neck formation and particles forming distinguishable grain boundaries, compatible with an intermediary stage of densification. On the other hand, the SEM images of samples 1Fe–CGO and 5Fe–CGO (Fig. 5b and c) show considerably higher densification (~90% relative density) compared to CGO at the same temperature. This result confirms the effectiveness of Fe as a sintering aid. The addition of the sintering aid had a marked effect on the grain size of the ceramics. The calculated average grain size values for the CGO, 1Fe–CGO, and 5Fe–CGO samples were 0.018 ± 0.021 μm, 0.24 ± 0.14 μm and 0.37 ± 0.19 μm, respectively.

Fig. 6 shows the SEM images of the polished and thermally etched samples sintered at 1400 °C. Increasing the sintering temperature of the CGO to 1400 °C had no significant effect on the porosity as compared to the sample sintered at 1200 °C (Fig. 5). Such results indicate that the critical pore size was exceeded in intermediate sintering stages, preventing further densification with increasing temperature. The SEM images in Fig. 6b and c show that the 1Fe–CGO and 5Fe–CGO samples have achieved a higher densification at this temperature (>95% relative density). The 1Fe–CGO sample exhibited little residual porosity, mostly located at the triple points, while in the 5Fe–CGO sample, the pores were eliminated. The 1Fe–CGO sample presented an average grain size of 2.87 ± 0.98 μm and the 5Fe–CGO sample an average of 2.69 ± 1.08 μm, representing a ten-fold increase in grain size compared to the sample sintered at 1200 °C. A similar grain growth for both samples is consistent with the shrinkage profiles (Fig. 4) that show the maximum shrinkage rate and final stage of sintering activity at the same temperature (1270 °C), as well as a similar intensity of the peak related to the maximum shrinkage rate.

In Fig. 6, a distinctive contrast difference between some grains reveals darker grains in the Fe-doped samples (indicated by yellow arrows). Such dark grains increased with

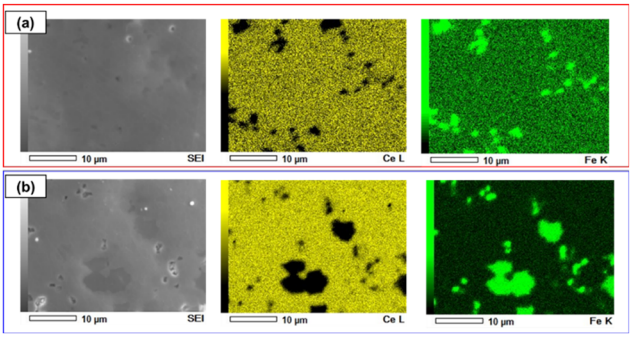

Fig. 7 SEM images of polished and thermally etched cross-sections and corresponding EDX elemental mapping of (a) 1Fe–CGO and (b) 5Fe–CGO, both sintered at 1400 °C.

increased Fe doping and were absent in the samples sintered at 1200 °C (Fig. 5). The EDS analysis was carried out, and the resulting elemental distribution maps of the Fe-doped samples are shown in Fig. 7. A clear correspondence between the EDS and phase contrast in SEM images evidenced that dark grains are isolated Fe-rich grains formed in both 1Fe–CGO and 5Fe–CGO sintered samples. The calculated volumetric fraction of Fe-rich grains was estimated at 1 and 5 vol% for the 1Fe–CGO and 5Fe–CGO samples, respectively.

The formation of a second Fe-rich phase at 1400 °C indicates that the system reached the grain boundary saturation.[36] With increasing sintering temperature, as the grains grow, the grain boundary specific area decreases and the net concentration of dopant increases.[59] The increased dopant concentration rapidly increases the concentration of solute atoms segregated at the GBs which eventually results in the formation of a Fe-rich second phase.[60,61] The secondary phase was further observed by the XRD of the samples heated to 1400 °C shown in supplementary Fig. S1,† where additional peaks are observed for the Fe-doped samples and are attributed to the gadolinium iron oxide phase (ICDD 00-048-0077). Such peaks were not observed in the samples treated at 1200 °C, in which the grain boundary surface was high enough to promote the solubility of segregated iron.

The influence of Fe doping on the electrical properties of the CGO samples was measured by EIS. Fig. 8 shows the EIS diagrams of the samples at 300 °C under synthetic air. The EIS diagrams of studied samples are qualitatively similar, showing a small semicircle at the high-frequency end, with relaxation frequency $> 10^6$ Hz, and a second semicircle at intermediary frequencies (10^5–10^2 Hz) that is convoluted with the electrode polarization spike at the low-frequency end. The EIS diagrams can be fitted with the equivalent circuit $(R_bCPE_b)(R_{gb}CPE_{gb})$, where $R_{(b,gb)}$ and $CPE_{(b,gb)}$ represent the resistance (R) and capacitive components (constant phase element, CPE) of the bulk (b) and grain boundary (gb). Fe-doped samples with high apparent density (~95%) have lower total resistivity compared to the CGO sample. Such a decrease is mainly observed in the R_{gb} component, which is considerably larger in CGO than in the Fe-doped samples. The bulk resistances of all samples are in the same range revealing that the Fe had a less marked effect on the bulk conductivity of the Fe-doped samples. Nevertheless, 5Fe–CGO has the smallest R_b value. The observed properties agree with the microstructure of the samples shown in Fig. 6 and previous EIS data on porous solid electrolytes, in which the blocking of charge carriers is mainly observed in the grain boundary frequency range.[62]

The similar microstructure, grain size, and density of samples sintered at 1400 °C allow the evaluation of the CGO ionic conductivity with increasing Fe addition. The EIS measured under 4% H_2/Ar (not shown) was used to assess the performance of the Fe-doped samples at a reducing atmosphere. Under low oxygen partial pressure (p_{O_2}), the bulk (R_b) and GB resistances (R_{gb}) exhibit a mixed ionic–electronic

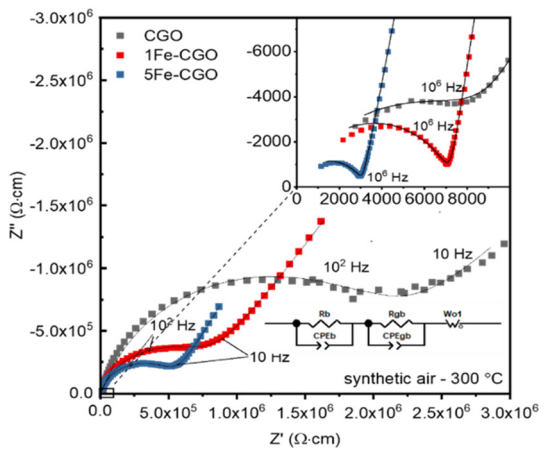

Fig. 8 Nyquist plots of CGO and Fe-doped CGO samples sintered at 1400 °C measured under a synthetic air flow at 300 °C. Inset shows the expanded high-frequency region.

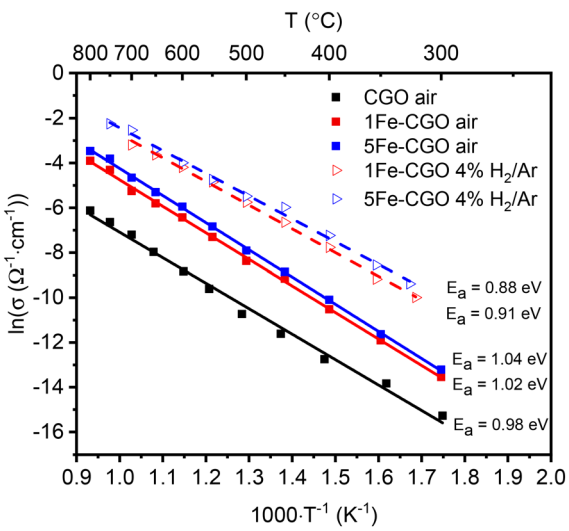

Fig. 9 Arrhenius plots of the total electrical conductivity of CGO and Fe-doped CGO samples sintered at 1400 °C measured under a synthetic air flow and 4% H_2/Ar.

conductivity.[63,64] The increase in Fe content decreased both bulk and GB resistances at low p_{O_2}. Under a reducing atmosphere, iron oxide (Fe_2O_3) has been reported to reduce to Fe_3O_4 at 300 °C and then to metallic Fe at 450 °C.[65] The secondary Fe-rich phase, observed in Fig. 7, is prone to reduce and therefore exhibiting a relatively high electronic conductivity, which also decreases the bulk resistance of the Fe-doped CGO samples.

Arrhenius plots of the total conductivity obtained under synthetic air and 4% H_2/Ar are shown in Fig. 9. All samples exhibited Arrhenius-type thermally activated temperature dependence of the total electrical conductivity. At high p_{O_2} (synthetic air), the electrical conductivity is mostly ionic, whereas in 4% H_2/Ar, a large fraction of electronic charge carriers develops. At high temperatures and low p_{O_2}, ceria exhibits an n-type conductivity due to its double valence state.[66–68] The higher conductivity of ceria under hydrogen is related to the mixed ionic–electronic properties of the ceria-based materials. The calculated activation energies of CGO are comparable to previously reported values[69] and have no significant dependence on the Fe content. The addition of Fe increases the density of the samples, and therefore increases the total conductivity of the samples sintered at 1400 °C.

Conclusions

The distribution of Fe added as a sintering aid in gadolinia-doped ceria was investigated. Iron segregates preferentially at the solid–solid interface (grain boundaries) of agglomerated ceria nanoparticles rather than in the bulk as a solid solution. The segregated iron species at the grain boundary are the ones to promote grain size decrease and faster densification of CGO. The results revealed a surface excess of 0.139 μmol m^{-2} for 5 mol% Fe-doped CGO, which is associated with an increase in the specific grain boundary area. The sintering studies showed that Fe promoted the densification of CGO at a lower temperature than that of undoped ceria–gadolinia. Grain boundary saturation of the additive was observed with increasing sintering temperature due to the decrease in the specific GB area, leading to the formation of Fe-rich grains at 1400 °C. The effect of the dopant on the electrical properties was mainly attributed to the increased density of Fe-doped samples. Iron doping had a small effect on the mixed ionic electronic properties of the CGO samples.

Author contributions

Marina Machado: investigation, writing. Andre Silva: investigation, writing. Leticia P. R. Moraes: investigation. Lays N. Rodrigues: investigation. Lorena Caliman: investigation. Douglas Gouvêa: conceptualization, supervision, funding acquisition and Fabio C. Fonseca: conceptualization, supervision, writing – review & editing, funding acquisition, project administration.

Conflicts of interest

There are no conflicts to declare.

Acknowledgements

The authors are grateful for the support of the Brazilian National Council for Scientific and Technological Development CNPq Sis-H2 grant no. 407967/2022-2 and Fundação de Amparo à Pesquisa do Estado de São Paulo (FAPESP) grants no. 2019/21159-4, 2019/04499-6, 2017/11937-4, 2014/09087-4, 2019/10109-6, and 2022/06295-1. FCF and DG are CNPq fellows.

Notes and references

1 D. J. L. Brett, A. Atkinson, N. P. Brandon and S. J. Skinner, *Chem. Soc. Rev.*, 2008, **37**, 1568.
2 B. Steele, *Solid State Ionics*, 2000, **129**, 95–110.
3 A. Atkinson, *Solid State Ionics*, 1997, **95**, 249–258.
4 F.-Y. Wang, S. Chen and S. Cheng, *Electrochem. Commun.*, 2004, **6**, 743–746.
5 J. G. Lee, J. H. Park and Y. G. Shul, *Nat. Commun.*, 2014, **5**, 4045.
6 N. Sammes, *Solid State Ionics*, 1997, **100**, 39–44.
7 M. Mogensen, *Solid State Ionics*, 2000, **129**, 63–94.
8 G. Postole, K. Girona, J. Toyir, A. Kaddouri and P. Gélin, *Fuel Cells*, 2012, **12**, 275–287.
9 B. L. Augusto, F. B. Noronha, F. C. Fonseca, F. N. Tabuti, R. C. Colman and L. V. Mattos, *Int. J. Hydrogen Energy*, 2014, **39**, 11196–11209.
10 M. Dubey, S. Wadhwa, A. Mathur and R. Kumar, *Appl. Surf. Sci. Adv.*, 2022, **12**, 100340.
11 Z. Gao, D. Kennouche and S. A. Barnett, *J. Power Sources*, 2014, **260**, 259–263.
12 R. Fuentes and R. Baker, *Int. J. Hydrogen Energy*, 2008, **33**, 3480–3484.
13 S. L. Reis, E. C. C. Souza and E. N. S. Muccillo, *Solid State Ionics*, 2011, **192**, 172–175.
14 L. P. R. Moraes, M. Machado, L. N. Rodrigues, Z. Sun, D. Marani and F. C. Fonseca, *J. Alloys Compd.*, 2023, **967**, 171766.
15 D. Z. De Florio, V. Esposito, E. Traversa, R. Muccillo and F. C. Fonseca, *J. Therm. Anal. Calorim.*, 2009, **97**, 143–147.
16 T. S. Rodrigues, A. B. L. de Moura, F. A. e Silva, E. G. Candido, A. G. M. da Silva, D. C. de Oliveira, J. Quiroz, P. H. C. Camargo, V. S. Bergamaschi, J. C. Ferreira, M. Linardi and F. C. Fonseca, *Fuel*, 2019, **237**, 1244–1253.
17 J. Guerrero-Caballero, T. Kane, N. Haidar, L. Jalowiecki-Duhamel and A. Löfberg, *Catal. Today*, 2019, **333**, 251–258.
18 A. Sin, *Solid State Ionics*, 2004, **175**, 361–366.
19 J.-G. Cheng, S.-W. Zha, J. Huang, X.-Q. Liu and G.-Y. Meng, *Mater. Chem. Phys.*, 2003, **78**, 791–795.
20 V. Esposito, A. Kabir, M. Rosa, N. V. Nong, T. S. Rodrigues, L. N. Rodrigues, M. F. S. Machado, L. P. R. Moraes, D. Marani and F. C. Fonseca, *CrystEngComm*, 2019, **21**, 4025–4029.

21 L. Miao, J. Hou, K. Dong and W. Liu, *Int. J. Hydrogen Energy*, 2019, **44**, 5447–5453.
22 S. Taub, R. E. A. Williams, X. Wang, D. W. McComb, J. A. Kilner and A. Atkinson, *Acta Mater.*, 2014, **81**, 128–140.
23 I. Shajahan, H. P. Dasari and P. Govardhan, *Mater. Chem. Phys.*, 2020, **240**, 122211.
24 M.-F. Han, S. Zhou, Z. Liu, Z. Lei and Z.-C. Kang, *Solid State Ionics*, 2011, **192**, 181–184.
25 A. K. Baral, H. P. Dasari, B.-K. Kim and J.-H. Lee, *J. Alloys Compd.*, 2013, **575**, 455–460.
26 J. Nicholas and L. Dejonghe, *Solid State Ionics*, 2007, **178**, 1187–1194.
27 T. H. Santos, J. P. F. Grilo, F. J. A. Loureiro, D. P. Fagg, F. C. Fonseca and D. A. Macedo, *Ceram. Int.*, 2018, **44**, 2745–2751.
28 S. Y. Toor and E. Croiset, *Ceram. Int.*, 2020, **46**, 1148–1157.
29 Y. Zheng, M. Zhou, L. Ge, S. Li, H. Chen and L. Guo, *J. Alloys Compd.*, 2011, **509**, 546–550.
30 C. J. Fu, Q. L. Liu, S. H. Chan, X. M. Ge and G. Pasciak, *Int. J. Hydrogen Energy*, 2010, **35**, 11200–11207.
31 J. Cheng, C. Tian and J. Yang, *J. Mater. Sci.: Mater. Electron.*, 2019, **30**, 16613–16620.
32 J. H. Choi, T. Lee, M. Choi, Y.-S. Yoo, S.-W. Baek and J. Bae, *Int. J. Hydrogen Energy*, 2010, **35**, 4285–4291.
33 A. M. Dayaghi, K. J. Kim, S. Kim, J. Park, S. J. Kim, B. H. Park and G. M. Choi, *J. Power Sources*, 2016, **324**, 288–293.
34 H. J. Avila-Paredes and S. Kim, *Solid State Ionics*, 2006, **177**, 3075–3080.
35 D. Pérez-Coll, P. Núñez, J. C. C. Abrantes, D. P. Fagg, V. V. Kharton and J. R. Frade, *Solid State Ionics*, 2005, **176**, 2799–2805.
36 R. H. R. Castro, *Cerâmica*, 2019, **65**, 122–129.
37 P. Wynblatt, G. S. Rohrer and F. Papillon, *J. Eur. Ceram. Soc.*, 2003, **23**, 2841–2848.
38 A. L. Da Silva, J. Bettini, A. A. Bernardes, R. H. R. Castro and D. Gouvêa, *J. Phys. Chem. C*, 2023, **127**, 1536–1547.
39 A. L. da Silva, D. N. F. Muche, L. B. Caliman, J. Bettini, R. H. R. Castro, A. Navrotsky and D. Gouvêa, *J. Phys. Chem. C*, 2019, **123**, 4949–4960.
40 M. F. S. Machado, L. P. R. Moraes, N. K. Monteiro, V. Esposito, D. Z. de Florio, D. Marani and F. C. Fonseca, *ECS Trans.*, 2017, **78**, 387–394.
41 D. C. O. S. Neves, A. L. da Silva, R. C. de Oliveira Romano and D. Gouvêa, *J. Eur. Ceram. Soc.*, 2020, **40**, 5959–5966.
42 A. L. Da Silva, L. Wu, L. B. Caliman, R. H. R. Castro, A. Navrotsky and D. Gouvêa, *Phys. Chem. Chem. Phys.*, 2020, **22**, 15600–15607.
43 F. C. Fonseca and R. Muccillo, *Solid State Ionics*, 2004, **166**, 157–165.
44 A. L. da Silva, D. Hotza and R. H. R. Castro, *Appl. Surf. Sci.*, 2017, **393**, 103–109.
45 L. Wu, S. Dey, M. Gong, F. Liu and R. H. R. Castro, *J. Phys. Chem. C*, 2014, **118**, 30187–30196.
46 A. A. Bernardes, L. B. Caliman, A. L. da Silva, J. Bettini, K. L. Guimarães and D. Gouvea, *J. Am. Ceram. Soc.*, 2020, **103**, 2835–2844.
47 H. Zhang and J. F. Banfield, *Chem. Rev.*, 2014, **114**, 9613–9644.
48 D. Gouvêa, D. C. C. do Rosário and L. B. Caliman, *J. Am. Ceram. Soc.*, 2017, **100**, 4331–4340.
49 R. H. R. Castro, *Mater. Lett.*, 2013, **96**, 45–56.
50 R. H. R. Castro and D. Gouvêa, *J. Am. Ceram. Soc.*, 2016, **99**, 1105–1121.
51 B. Cela, D. A. De MacEdo, G. L. De Souza, A. E. Martinelli, R. M. Do Nascimento and C. A. Paskocimas, *J. Power Sources*, 2011, **196**, 2539–2544.
52 Z. Wang, Y. Zeng, C. Li, Z. Ye, L. Cao and Y. Zhang, *Ceram. Int.*, 2018, **44**, 10328–10334.
53 K. Neuhaus, R. Dolle and H.-D. Wiemhöfer, *J. Electrochem. Soc.*, 2020, **167**, 044507.
54 L. R. K. T. Jacob, S. Raj and L. Rannesh, *Int. J. Mater. Res.*, 2007, **98**, 776–779.
55 R. A. M. P. de Oliveira, A. L. da Silva, L. B. Caliman and D. Gouvêa, *Ceram. Int.*, 2020, **46**, 10555–10560.
56 R. H. R. Castro and D. Gouvêa, *J. Am. Ceram. Soc.*, 2016, **99**, 1105–1121.
57 V. Esposito, D. W. Ni, Z. He, W. Zhang, A. S. Prasad, J. A. Glasscock, C. Chatzichristodoulou, S. Ramousse and A. Kaiser, *Acta Mater.*, 2013, **61**, 6290–6300.
58 R. L. Coble, *J. Appl. Phys.*, 1961, **32**, 787–792.
59 D. N. F. Muche, A. L. da Silva, K. Nakajima, D. Gouvêa and R. H. R. Castro, *Appl. Surf. Sci.*, 2020, **529**, 147145.
60 F. Liu and R. Kirchheim, *J. Cryst. Growth*, 2004, **264**, 385–391.
61 F. Teocoli, D. W. Ni, S. Sanna, K. Thydén, F. C. Fonseca and V. Esposito, *J. Mater. Chem. A*, 2015, **3**, 17135–17143.
62 D. Pérez-Coll, E. Sánchez-López and G. C. Mather, *Solid State Ionics*, 2010, **181**, 1033–1042.
63 V. V. Kharton, A. V. Kovalevsky, A. P. Viskup, A. L. Shaula, F. M. Figueiredo, E. N. Naumovich and F. M. B. Marques, *Solid State Ionics*, 2003, **160**, 247–258.
64 D. P. Fagg, V. V. Kharton and J. R. Frade, *J. Electroceram.*, 2002, **9**, 199–207.
65 P. Sudarsan and S. B. Krishnamoorthy, *Mater. Res. Bull.*, 2018, **100**, 446–457.
66 W. Lai and S. M. Haile, *J. Am. Ceram. Soc.*, 2005, **88**, 2979–2997.
67 S. Wang, T. Kobayashi, M. Dokiya and T. Hashimoto, *J. Electrochem. Soc.*, 2000, **147**, 3606.
68 S. Taub, K. Neuhaus, H. D. Wiemhöfer, N. Ni, J. A. Kilner and A. Atkinson, *Solid State Ionics*, 2015, **282**, 54–62.
69 H. Inaba, *Solid State Ionics*, 1996, **83**, 1–16.